

Article

Ultrathin ZnS Electron Transport Layer Enables Efficient p-Si Photocathode for Photoelectrochemical Hydrogen Production

Yanming Li^{1,†}, Jianjun Jiang^{1,†}, Chenglong Ding¹, Hao Wang¹, Yequan Xiao^{2,*},
Jingfu He^{1,*} and Changli Li^{1,*}¹ School of Materials, Shenzhen Campus of Sun Yat-sen University, Shenzhen 518107, China² Hubei Provincial Engineering Research Center for Solar Energy High-value Utilization and Green Conversion, College of Materials Science and Engineering, China Three Gorges University, Yichang 443002, China

* Correspondence: xiaoyequan@ctgu.edu.cn (Y.X.); hejf27@mail.sysu.edu.cn (J.H.); lichli5@mail.sysu.edu.cn (C.L.)

† These authors contributed equally to this work.

How To Cite: Li, Y.; Jiang, J.; Ding, C.; et al. Ultrathin ZnS Electron Transport Layer Enables Efficient p-Si Photocathode for Photoelectrochemical Hydrogen Production. *Low-Dimensional Materials* 2025, 1(1), 4. <https://doi.org/10.53941/ldm.2025.100004>

Received: 28 September 2025

Revised: 4 November 2025

Accepted: 10 November 2025

Published: 17 November 2025

Abstract: Silicon (Si) is considered one of the most promising semiconductor materials for photocathodes in photoelectrochemical (PEC) hydrogen production, owing to its narrow bandgap, excellent optoelectronic properties, and earth abundance. To achieve efficient charge separation and transport during PEC operation, selecting an appropriate electron transport layer (ETL) on p-Si is essential for constructing a buried junction. However, the development of p-Si heterojunction photocathodes with high photovoltage and efficient interfacial carrier transfer is often hindered by unfavorable band alignment between the absorber and ETL. In this study, an ultrathin ZnS layer was employed as the ETL for p-Si due to its low electron affinity, which enables a high theoretical photovoltage for the heterojunction photocathode. Furthermore, a sulfidation process was applied to passivate the ZnS layer. After sulfidation at 400 °C, the p-Si/ZnS/Pt photocathode exhibited a positive onset potential of 0.5 V_{RHE} and an ABPE of 2.3% at 0.2 V_{RHE}. EDS and XPS analyses confirmed the removal of oxidized species and the formation of sulfur vacancies in suitable amounts, which led to optimized carrier concentration and barrier height, thereby enhancing charge transfer kinetics and suppressing carrier recombination.

Keywords: p-Si photocathode; ultrathin ZnS layer; sulfidation; sulfur vacancies; PEC hydrogen production

1. Introduction

Photoelectrochemical (PEC) water splitting is an attractive and environmentally friendly approach for converting solar energy into storable hydrogen. Achieving highly efficient and stable PEC hydrogen evolution reaction (HER) requires rational design of the photocathode [1–4]. An ideal photoelectrode should efficiently absorb a broad solar spectrum and incorporate an effective p-n junction or solid/liquid interface to facilitate the extraction and transport of photogenerated carriers while providing sufficient photovoltage to reduce external energy input. Silicon (Si) has long attracted attention due to its high carrier mobility, narrow bandgap (1.12 eV), and suitable conduction band position (more negative than 0 V vs. RHE) [5]. Despite extensive efforts to develop Si-based photocathodes with various diverse architectures [6], achieving a cost-effective Si heterojunction system that simultaneously ensures high PEC performance and efficient electron-transfer/catalytic interfaces remains elusive. The primary bottleneck lies in silicon's intrinsically low photovoltage, which necessitates substantial external bias to sustain overall water splitting.



Copyright: © 2025 by the authors. This is an open access article under the terms and conditions of the Creative Commons Attribution (CC BY) license (<https://creativecommons.org/licenses/by/4.0/>).

Publisher's Note: Scilight stays neutral with regard to jurisdictional claims in published maps and institutional affiliations.

Forming an appropriate built-in electric field is essential for accelerating carrier separation and providing sufficient photovoltage to drive efficient PEC reactions. Strategies such as intrinsic thin-layer heterojunctions (HIT) [7] and metal-insulator-semiconductor (MIS) structures [8–10] can enhance photovoltage, but both approaches face limitations: HIT requires costly deposition and shows low carrier separation efficiency in near-neutral electrolytes, while MIS structures may impede light absorption due to the metal layer. An alternative is to construct a p-n heterojunction by depositing an n-type ETL on p-Si, where careful energy band alignment is critical. A large Fermi level difference between p-Si and the ETL is necessary to achieve high photovoltage and efficient charge separation.

Recent studies have demonstrated that ultrathin high-k dielectric layers, such as HfO₂ can provide excellent surface passivation and significantly improve the open-circuit voltage and stability of Si photocathodes [11]. Meanwhile, carrier-selective, passivated contacts such as poly-Si/SiO_x structures yield high photovoltage and outstanding selectivity but often require complex fabrication and may cause parasitic absorption or interfacial losses [12]. Among diverse ETL candidates such as oxides, sulfides, and nitrides [13–15], metal sulfides stand out owing to their favorable band alignment, high electron affinity, and rapid carrier dynamics [16]. While CdS has been widely applied, its relatively low bandgap (~2.4 eV) constrains solar spectrum utilization. In contrast, wide-bandgap ZnS (>3.2 eV) is transparent to visible light, enabling efficient photon harvesting by the underlying p-type absorber, while its deep Fermi level supports high photovoltage in p-Si/ZnS heterojunctions. Furthermore, ZnS offers excellent chemical stability, functioning both as a protective layer and as a facilitating interfacial charge transfer [17,18]. Its facile chemical tunability through sulfidation to engineer sulfur vacancies. This multifunctional ZnS layer thus acts as a transparent electron transport and passivation layer, effectively balancing interfacial passivation and charge-transfer efficiency in buried-junction p-Si photocathodes. However, the large conduction band offset (~1.0 eV) between ZnS and p-Si presents a barrier for electron extraction, requiring precise optimization of ZnS thickness and defect states to promote tunneling while minimizing recombination losses.

In this study, ZnS was selected as an ETL on p-Si for PEC water splitting. The Fermi level of ZnS (~-4 eV with respect to the vacuum level), sufficiently negative relative to that of p-Si, favors enhanced photovoltage. Systematic thickness optimization revealed that a 5 nm ZnS layer strikes an optimal balance, providing a high barrier height and efficient charge transfer while minimizing interfacial transfer resistance. To further tune sulfur vacancies and suppress photogenerated carrier recombination, a post-deposition sulfidation treatment was applied to the ZnS layer. Electrochemical analyses, including Mott-Schottky measurements, reveal the evolution of flat-band potential, bandgap, and charge-transfer resistance before and after sulfidation. Following 400 °C sulfidation, the p-Si/ultrathin-ZnS/Pt photocathode achieves an onset potential of 0.5 V versus a reversible hydrogen electrode (V_{RHE}) and an ABPE of 2.3% at 0.2 V_{RHE}. These results demonstrate that integrating ultrathin ZnS with defect engineering constitutes an effective strategy for advancing high-performance PEC water-splitting devices.

2. Results and Discussion

Experimental details are provided in the Supporting Information. Buffer layers and Pt cocatalyst were deposited onto p-Si wafers via magnetron sputtering to construct Si-based photocathodes. Figure 1 shows the 500 nm × 500 nm surface morphology of p-Si, p-Si/ZnS, and p-Si/ZnS/Pt samples measured by atomic force microscopy (AFM). Pristine p-Si exhibited a peak-to-valley height of 2 nm and an average roughness of 0.272 nm (Figure 1a). After ZnS deposition, the average roughness slightly decreased to 0.231 nm (Figure 1b). Subsequent Pt deposition increased the peak-to-valley height to 1.3 nm and the average roughness to 0.357 nm (Figure 1c). These results confirm that both the ZnS buffer layer and Pt cocatalyst are uniformly deposited on p-Si, facilitating the formation of a homogeneous heterojunction for PEC water splitting.

The PEC performances of p-Si/Pt and p-Si/ZnS/Pt photocathodes were evaluated using a three-electrode cell in pH 5.7 phosphate buffer under AM1.5G simulated sunlight (100 mW/cm²). Figure 2a compares the performance of silicon-based photocathodes with and without an optimized ZnS buffer layer. The p-Si/Pt photocathode exhibited an onset potential of -0.02 V_{RHE} and a photocurrent below 15 mA/cm² at -0.6 V_{RHE}. Incorporation of as-prepared ZnS degraded performance (-0.1 V_{RHE} and ~5 mA/cm²), likely due to poor crystallinity serving as carrier recombination centers. Air annealing partially recovered performance, shifting the onset potential by ~160 mV (0.14 V_{RHE}) and increasing the photocurrent above 20 mA/cm². However, the photovoltage remained lower than the theoretical Fermi level difference between p-Si and ZnS, likely due to oxidized ZnS species that altered the bandgap and absorption [19].

To optimize the ZnS layer, a sulfidation treatment was introduced, and the effect of sulfurization temperature on photocathode performance was systematically examined (Figure 2b). Compared with air-annealed samples, sulfurized photocathodes exhibited positive shifts in onset potential. At 300 °C, the p-Si/ZnS/Pt photocathode

achieved $\sim 18 \text{ mA/cm}^2$ at $-0.3 \text{ V}_{\text{RHE}}$ and an onset potential of $\sim 0.3 \text{ V}_{\text{RHE}}$. However, annealing temperatures above $450 \text{ }^\circ\text{C}$ caused significant photocurrent loss, most likely due to sulfur depletion [20]. The optimal performance was obtained at $400 \text{ }^\circ\text{C}$, where the onset potential reached $0.5 \text{ V}_{\text{RHE}}$ and a photocurrent approached $\sim 32 \text{ mA/cm}^2$ at $-0.3 \text{ V}_{\text{RHE}}$. EDS analysis confirmed that the sulfurization temperature strongly affects ZnS stoichiometry (Supplementary Materials Figure S2). The S:Zn ratios of samples at 300, 350, 400, 450, and $500 \text{ }^\circ\text{C}$ were 1.5, 1.0, 0.8, 0.59, and 0.56, respectively, showing a progressive decrease in sulfur content with increasing temperature, indicating a systematic loss of sulfur. Such variation in stoichiometry is directly tied to defect states. In metal sulfides, sulfur vacancies act as electron-donor defects, promoting charge separation and suppressing electron-hole recombination [20,21]. Yet, when the vacancy concentration becomes excessive, recombination dominates, ultimately impairing device performance.

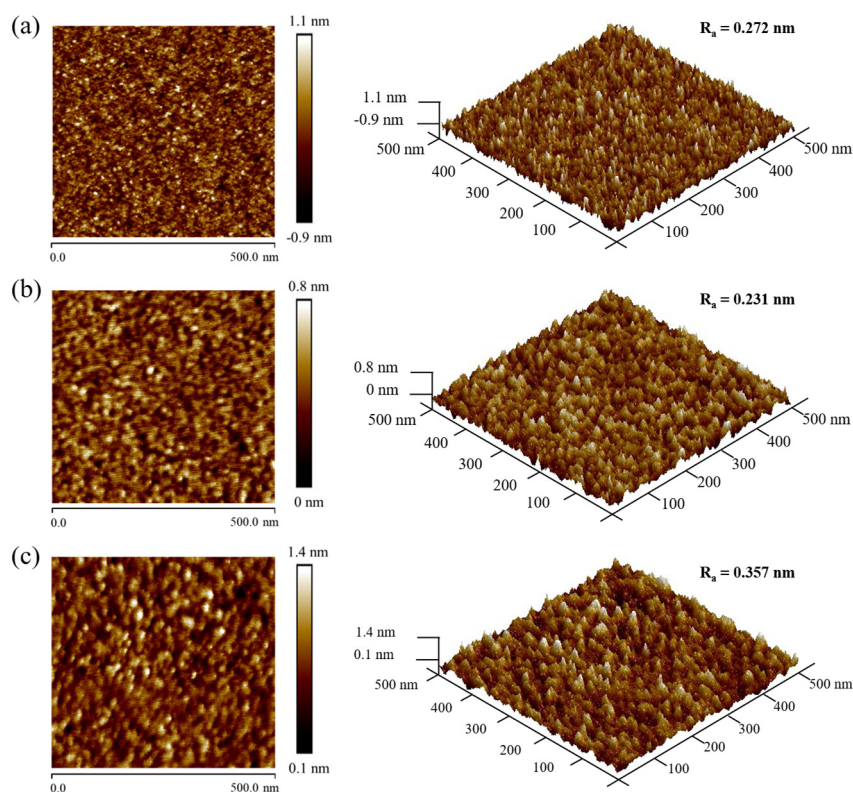


Figure 1. AFM images of p-Si (a); p-Si/ZnS (b); and p-Si/ZnS/Pt (c), R_a represents average surface roughness.

A thick buffer layer typically increases carrier transfer resistance, thereby accelerating photoinduced carrier recombination and reducing PEC performance. To investigate this effect, we further examined the influence of ZnS thickness under the optimized $400 \text{ }^\circ\text{C}$ sulfidation condition (Figure 2c). The p-Si/ZnS-2 nm/Pt photocathode exhibited an onset potential of $\sim 0.5 \text{ V}_{\text{RHE}}$, suggesting that a thin ZnS layer favors electron transport. However, its low fill factor suggests limited passivation and poor interfacial separation. Increasing the thickness to 5 nm improved both passivation and charge transfer, yielding the best performance with an onset potential of $\sim 0.5 \text{ V}_{\text{RHE}}$ and a photocurrent of 32 mA/cm^2 , representing the optimal balance between carrier transport and passivation. Further thickening to 10 nm caused a sharp performance decline, likely due to unfavorable band bending in thicker ZnS layers, which hinders electron extraction to the co-catalyst [22].

By jointly optimizing sulfidation temperature and ZnS thickness, a high-performance p-Si/ultrathin-ZnS/Pt photocathode was obtained. Relative to air-annealed samples, the sulfidated electrode exhibited a positive shift of $\sim 400 \text{ mV}$ in onset potential and a 1.5-fold increase in photocurrent ($\sim 32 \text{ mA/cm}^2$ at $-0.3 \text{ V}_{\text{RHE}}$). Stability test confirmed that $\sim 66\%$ of the photocurrent was retained after 1 h of continuous operation at 0 V_{RHE} under simulated sunlight (Supplementary Materials Figure S3), demonstrating robust stability for sustained PEC hydrogen production. ABPE values (Figure 2d) further underscored the impact of sulfidation, with the maximum ABPE increasing nearly 20-fold from 0.12% for air-annealed photocathodes to 2.3% after sulfidation. These results confirm that the optimized p-Si/ultrathin-ZnS/Pt photocathode combines high efficiency and stability, emphasizing the critical role of sulfidation in enhancing PEC hydrogen evolution. The Faradaic efficiency (FE) for hydrogen (H_2) production on the p-Si/ZnS/Pt photocathode remains close to 100% at potentials above 0 V vs.

RHE (Supplementary Materials Figure S9). However, the FE gradually decreases at more negative potentials, which can be attributed to the intensified reaction at the photoelectrode surface. The EDS mapping results show that the Pt/O atomic ratio decreases from 1:3 to 1:5.6 after 1 h of operation (Supplementary Materials Figure S10), confirming substantial Pt leaching. XPS analysis further verifies notable chemical changes in the surface composition following the stability test (Supplementary Materials Figure S11). Such degradation generates surface defects that facilitate charge recombination rather than efficient carrier separation, resulting in parasitic charge loss and a gradual decline in photocurrent density.

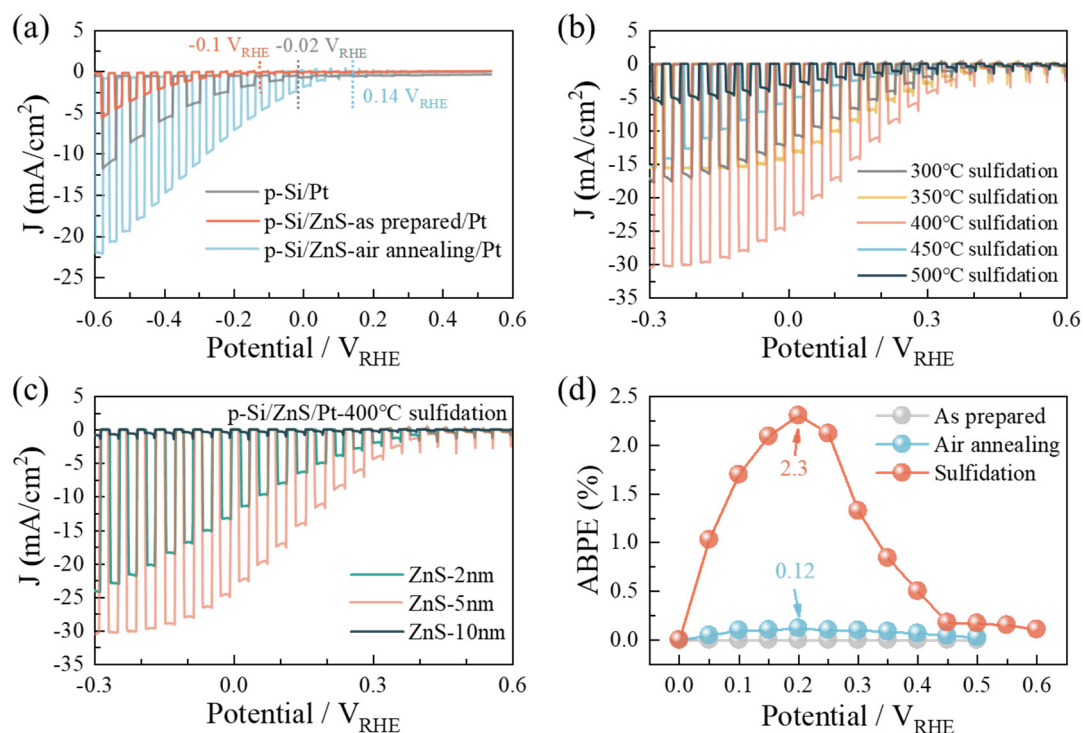


Figure 2. (a) PEC performance of p-Si/Pt, p-Si/ZnS-as prepared/Pt and p-Si/ZnS-air annealing/Pt electrodes; (b) PEC performance of p-Si/ZnS/Pt under different sulfidation temperatures; (c) Comparison in the PEC performance of p-Si/ thin ZnS/Pt with different thicknesses; (d) ABPE (Applied Bias Photon-to-current Efficiency, ABPE) of p-Si/ ZnS/Pt photocathode with different annealing processes (as prepared, air annealing, and sulfidation).

To evaluate the generality of the sulfidation process, two commonly used n-type sulfide buffer layers (CdS and In₂S₃) were extended sulfidation. For both materials, the optimal sulfidation temperature was identified as 200 °C (Supplementary Materials Figure S4a,d). After sulfidation treatment, the onset potentials of p-Si/CdS/Pt and p-Si/In₂S₃/Pt photocathodes shifted positively to 0.45 V_{RHE} and 0.3 V_{RHE}, respectively (Supplementary Materials Figure S4b,e). Elemental analysis confirmed corresponding variations in sulfur content (Supplementary Materials Figure S5). ABPE values were also significantly enhanced (Supplementary Materials Figure S4c,f), demonstrating that an appropriate concentration of sulfur vacancies improves the electronic properties of ETLs. These findings indicate that sulfidation effectively passivates surface defects generated during conventional air annealing and broadly enhances PEC performance across different sulfide buffer layers.

Based on the above experimental results, different annealing conditions can effectively regulate the properties of ZnS and influence the PEC performance of the photoelectrode. To clarify this effect, we investigated ultrathin ZnS under different annealing processes using Mott-Schottky (MS), UV-vis, and XPS analyses. The as-prepared ZnS exhibited a flat-band potential of $-0.78 V_{RHE}$, which shifted positively by 0.1 V after air annealing, likely due to the formation of oxidized species. In contrast, sulfidation induced a negative shift in flat-band potential from $-0.67 V_{RHE}$ to $-0.92 V_{RHE}$, indicating the effective removal of oxidized compounds. As shown in Figure 3b, the bandgap of ZnS increased from 3.0 eV (as-prepared) to 3.2 eV (air-annealed) and 3.6 eV (sulfidated), reflecting changes in defects and chemical states. XPS analysis further confirmed these trends (Figure 3c,d). For as-prepared ZnS, the S 2p peaks at 161.8 eV and 163.0 eV correspond to S 2p_{3/2} and S 2p_{1/2} of ZnS [23], while the O 1s peak at 531.6 eV arises from adsorbed oxygen. Air annealing introduced lattice oxygen at 530.1 eV in addition to adsorbed oxygen (531.8 eV) [24], confirming oxygen incorporation into ZnS that acts as an impurity. Sulfidation eliminated the lattice oxygen signal (Figure 3d), suggesting that the bandgap increase originates from ZnO

reduction. Additionally, no obvious shift was observed in the Zn 2p peaks after sulfidation (Supplementary Materials Figure S6), whereas the S 2p peak exhibited a negative shift of 0.16 eV, indicative of sulfur vacancies [25]. Taken together, these results suggest that oxidized species influence both bandgap and carrier concentration, and that sulfidation improves carrier density by removing oxides and generating an optimal concentration of sulfur vacancies.

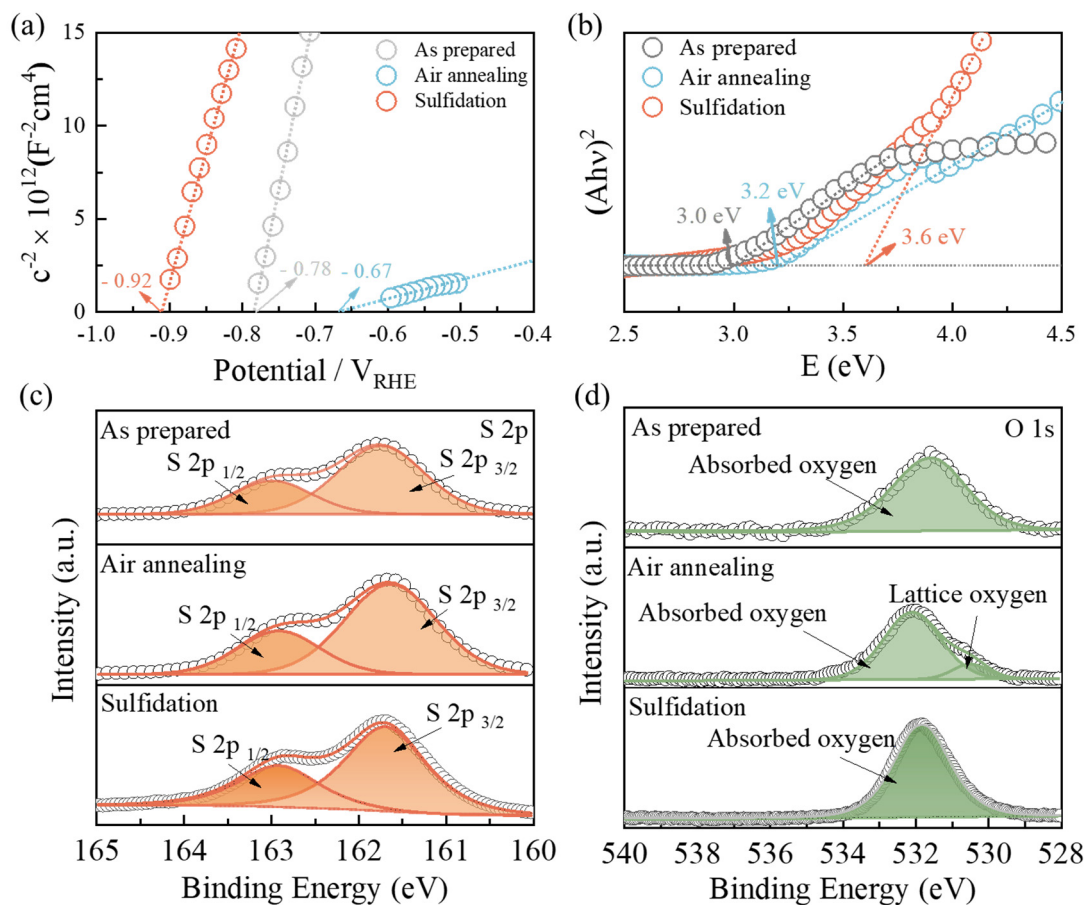


Figure 3. (a) Mott-Schottky plots and (b) UV-vis spectrums for ZnS with different annealing processes (as prepared, air annealing, and sulfidation). (c, d) XPS spectra of S 2p and O1s of ZnS with different annealing processes.

Similar trends were observed for CdS and In_2S_3 , as shown in Supplementary Materials Figure S7a–f. MS plots and UV-vis spectra confirmed changes in carrier concentration and bandgap after sulfidation. The flat-band potential shifted from $-0.20 V_{\text{RHE}}$ to $-0.40 V_{\text{RHE}}$ for CdS and from $-0.30 V_{\text{RHE}}$ to $-0.33 V_{\text{RHE}}$ for In_2S_3 . UV-vis spectra also showed band gaps in both CdS and In_2S_3 . XPS analysis verified the reduction of oxidized species in these sulfides after sulfidation (Supplementary Materials Figure S8), which likely contributes to the observed variations in bandgap and carrier concentration. In addition, Nyquist plots (Supplementary Materials Figure S7c,f) demonstrated improved charge transfer kinetics, highlighting the beneficial role of sulfidation.

Nyquist plots further illustrate the enhanced carrier transfer in sulfidated ZnS, as shown in Figure 4a. In a three-electrode configuration with p-Si/ZnS/Pt as the working photoelectrode, the solution resistance (R_s) remained comparable across as-prepared, air-annealed, and sulfidated ZnS. However, the charge transfer resistance (R_{ct}) decreased from 181.0 Ω (as-prepared) to 123.8 Ω (air-annealed) and 91.2 Ω (sulfidated) according to EIS fitting, demonstrating that sulfidation improves carrier transport and reduces transmission losses. The barrier height of p-Si/ZnS was evaluated via Mott-Schottky measurements in potassium ferricyanide solution, following previous reports [26]. The as-prepared ZnS exhibited a flat-band potential of 0.2 V and a calculated barrier height of 0.35 eV, likely due to imperfect crystallinity and unfavorable band alignment. Air annealing increased the flat-band potential to 0.55 V, while sulfidation further raised it to 0.7 V, indicating stronger band bending at the semiconductor/liquid junction and facilitating electron transfer and rapid hole extraction (Figure 4b). Calculated barrier heights under illumination (Figure 4c–e) confirm that sulfidation increases the effective barrier height. These results demonstrate that sulfidation improves barrier bending, thereby enhancing photovoltage and promoting efficient carrier separation.

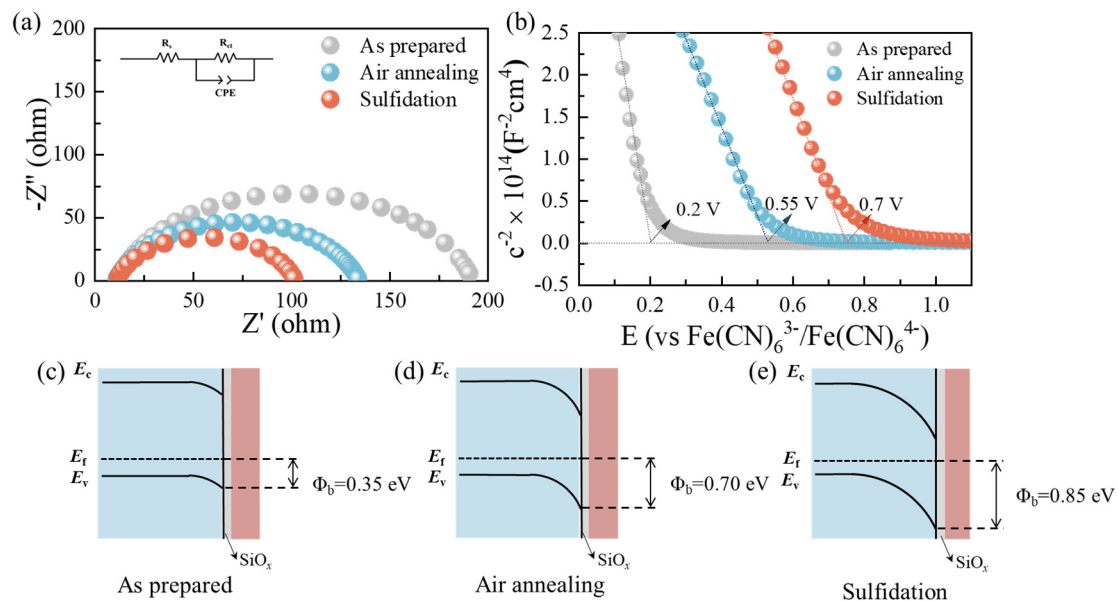


Figure 4. (a) Nyquist plots of p-Si/ultra-thin ZnS/Pt photocathode with different annealing processes at 0 V_{RHE} under simulated light; (b) Mott-Schottky plots of p-Si/ZnS/Pt with different annealing processes. (c–e) Band diagram of p-Si/ultra-thin ZnS/Pt photocathode with different annealing processes.

3. Conclusions

In this work, we introduce a sulfidation process on ultra-thin ZnS to passivate defects and construct an efficient Si-based photocathode. EDS and XPS analyses reveal that, compared with conventional ZnS air annealing, sulfidation removes oxidized species while introducing a controlled concentration of sulfur vacancies. By optimizing the sulfidation temperature and ZnS thickness, the resulting photocathodes exhibit an onset potential of $\sim 0.5 V_{\text{RHE}}$, a maximum photocurrent of $\sim 32 \text{ mA/cm}^2$, and a maximum ABPE of 2.31% at 0.2 V_{RHE} . Mott-Schottky and EIS measurements further confirm that sulfidation increases carrier concentration, enhances electron transfer kinetics, and suppresses recombination losses. Moreover, extending this process to other ETLs such as CdS and In_2S_3 demonstrates its universality, indicating that sulfidation can generally improve carrier transfer characteristics. These results highlight that integrating an ultrathin ZnS ETL with defect passivation provides a robust strategy for designing high-performance photocathodes and guiding related PEC hydrogen production research.

Supplementary Materials

The additional data and information can be downloaded at: <https://media.sciltp.com/articles/others/2511171424119458/LDM-25090121-Supplementary-Materials-FC-done.pdf>. Figure S1: Schematic diagram of the sulfidation process; Figure S2: S:Zn ratio under different sulfidation temperatures; Figure S3. Stability test of p-Si/ZnS/Pt electrode after 400 °C sulfidation. The test was carried out in phosphate buffer (pH 5.7) under AM 1.5 G illumination, with applied voltage of 0 V_{RHE} ; Figure S4: The effects of sulfidation treatment on the PEC performance of p-Si/CdS and p-Si/ In_2S_3 photocathodes. (a,d) The influence of sulfidation temperature of p-Si/CdS and p-Si/ In_2S_3 on PEC performance. (b,e) PEC performance comparison before and after the sulfidation process. (c,f) ABPE comparison of p-Si/CdS and p-Si/ In_2S_3 before and after the sulfidation process; Figure S5: S:Zn ratio variation of the mentioned ETLs after sulfidation. The S content increased after sulfidation process for all buffers. Before the sulfidation process, the S:Metal ratio is 0.56, 0.67, and 0.69 for ZnS, CdS, and In_2S_3 , indicating the unreasonable content of sulfur element. After the sulfidation process, this ratio increased to 0.80, 0.82, and 0.83; Figure S6: XPS binding energy variation of Zn 2p before and after sulfidation; Figure S7: The electronic and interfacial property changes of p-Si/CdS and p-Si/ In_2S_3 photocathodes before and after sulfidation. (a,d) Comparison of flat-band potential and carrier density of p-Si/CdS and p-Si/ In_2S_3 before and after sulfidation. (b,e) Comparison of absorption band gap of p-Si/CdS and p-Si/ In_2S_3 before and after sulfidation. (c,f) Comparison of electrochemical impedance spectroscopy of p-Si/CdS and p-Si/ In_2S_3 before and after sulfidation, measured at 0 V_{RHE} under AM 1.5 G simulated sunlight irradiation in phosphate buffer; Figure S8: XPS binding energy variation before and after sulfidation. (a–c) CdS; (d–f) In_2S_3 ; Figure S9: FE of the p-Si/ZnS/Pt-400 °C photocathode tested under 0.3 V, 0 V, and -0.3 V vs. RHE during PEC hydrogen evolution; Figure S10: The morphology changes of the p-Si/ZnS/Pt-400 °C photocathode before (a) and after (b) PEC hydrogen evolution under 0 V vs. RHE for 1 h.

The energy-dispersive X-ray spectroscopy (EDS) mapping images for the p-Si/ZnS/Pt-400 °C photocathode before (c,d) and after (e,f) PEC hydrogen evolution under 0 V vs. RHE for 1 h; Figure S11: High-resolution XPS spectra of the p-Si/ZnS/Pt photocathode before and after 1 h PEC hydrogen evolution at 0 V vs. RHE. (a) Pt 4f; (b) O 1s; (c) Zn 2p; and (d) S 2p. Slight changes in Pt intensity and S:Zn ratio, along with increased O 1s signal, indicate partial Pt dissolution and minor surface reoxidation/stoichiometry changes in ZnS after operation. References [27–32] are cited in the supplementary materials.

Author Contributions

C.L.: conceptualization, methodology, data curation, supervision, writing—reviewing and editing, project Administration, funding acquisition; J.H.: methodology, writing—review & Editing, supervision; Y.X.: writing—reviewing and editing, supervision; Y.L.: writing—original draft preparation, investigation, visualization; J.J.: investigation, visualization, validation; C.D.: investigation, visualization, writing—original draft preparation. H.W.: investigation, validation. All authors have read and agreed to the published version of the manuscript.

Funding

This work was supported by the Shenzhen Science and Technology Program (Nos. JCYJ20230807110809021 and JCYJ20240813151418025), Natural Science Foundation of Guangdong Province (Nos. 2022A1515010928 and 2023A1515030236).

Institutional Review Board Statement

Not applicable.

Informed Consent Statement

Not applicable.

Data Availability Statement

The data presented in this study are available from the corresponding author upon reasonable request.

Conflicts of Interest

The authors declare no conflict of interest.

Use of AI and AI-Assisted Technologies

No AI tools were utilized for this paper.

References

1. Li, C.; He, J.; Xiao, Y.; et al. Earth-Abundant Cu-Based Metal Oxide Photocathodes for Photoelectrochemical Water Splitting. *Energy Environ. Sci.* **2020**, *13*, 3269–3306.
2. Feng, C.; Faheem, M.B.; Fu, J.; et al. Fe-Based Electrocatalysts for Oxygen Evolution Reaction: Progress and Perspectives. *ACS Catal.* **2020**, *10*, 4019–4047.
3. Huang, Q.; Ye, Z.; Xiao, X. Recent Progress in Photocathodes for Hydrogen Evolution. *J. Mater. Chem. A* **2015**, *3*, 15824–15837.
4. Xiao, W.; Lin, H.; Lu, L.; et al. Elucidating the Origin of Positive Onset Potential and Low Photovoltage of CuBi₂O₄ Photocathode. *J. Catal.* **2025**, *450*, 116325.
5. Cheng, C.; Zhang, W.; Chen, X.; et al. Strategies for improving photoelectrochemical water splitting performance of Si-based electrodes. *Energy Sci. Eng.* **2022**, *10*, 1526–1543.
6. Li, Y.; Xiao, Y.; Wu, C.; et al. Strategies To Construct N-Type Si-Based Heterojunctions for Photoelectrochemical Water Oxidation. *ACS Mater. Lett.* **2022**, *4*, 779–804.
7. Wang, H.-P.; Sun, K.; Noh, S.Y.; et al. High-Performance a-Si/c-Si Heterojunction Photoelectrodes for Photoelectrochemical Oxygen and Hydrogen Evolution. *Nano Lett.* **2015**, *15*, 2817–2824.
8. Ji, L.; McDaniel, M.D.; Wang, S.; et al. A silicon-based photocathode for water reduction with an epitaxial SrTiO₃ protection layer and a nanostructured catalyst. *Nat. Nanotechnol.* **2014**, *10*, 84–90.
9. Li, Y.; Ding, C.; Li, Y.; et al. Engineering the SiO_x Interfacial Layer of Si-Based Metal-Insulator-Semiconductor Junction for Photoelectrochemical Hydrogen Production. *J. Catal.* **2024**, *434*, 115533.

10. Li, Y.; Ding, C.; Li, Y.; et al. Engineering the Inhomogeneity of Metal–Insulator–Semiconductor Junctions for Photoelectrochemical Methanol Oxidation. *ACS Appl. Mater. Interfaces* **2023**, *15*, 59403–59412.
11. Zhang, D.; Liang, W.; Sharma, A.; et al. Ultrathin HfO₂ Passivated Silicon Photocathodes for Efficient Alkaline Water Splitting. *Appl. Phys. Lett.* **2021**, *119*, 193901.
12. Sharma, A.; Duong, T.; Liu, P.; et al. Direct Solar to Hydrogen Conversion Enabled by Silicon Photocathodes with Carrier Selective Passivated Contacts. *Sustain. Energy Fuels* **2022**, *6*, 349–360.
13. Pérez-del-Rey, D.; Boix, P.P.; Sessolo, M.; et al. Interfacial Modification for High-Efficiency Vapor-Phase-Deposited Perovskite Solar Cells Based on a Metal Oxide Buffer Layer. *J. Phys. Chem. Lett.* **2018**, *9*, 1041–1046.
14. Moon, D.G.; Rehan, S.; Yeon, D.H.; et al. A Review on Binary Metal Sulfide Heterojunction Solar Cells. *Sol. Energy Mater. Sol. Cells* **2019**, *200*, 109963.
15. Yi, G.; Wang, Q.; Arbiol, J.; et al. Emerging Metal Oxide/Nitride Protection Layers for Enhanced Stability of Silicon Photoelectrodes in Photoelectrochemical Catalysis: Recent Advancements and Challenges. *Mater. Today Chem.* **2023**, *34*, 101795.
16. Wang, J.; Lin, S.; Tian, N.; et al. Nanostructured Metal Sulfides: Classification, Modification Strategy, and Solar—Driven CO₂ Reduction Application. *Adv. Funct. Mater.* **2020**, *31*, 2008008.
17. Chae, S.Y.; Park, S.J.; Han, S.G.; et al. Enhanced Photocurrents with ZnS Passivated Cu(In,Ga)(Se,S)₂ Photocathodes Synthesized Using a Nonvacuum Process for Solar Water Splitting. *J. Am. Chem. Soc.* **2016**, *138*, 15673–15681.
18. Wang, K.; Huang, D.; Yu, L.; et al. Environmentally Friendly Cu₂ZnSnS₄-Based Photocathode Modified with a ZnS Protection Layer for Efficient Solar Water Splitting. *J. Colloid Interface Sci.* **2019**, *536*, 9–16.
19. Patel, S.L.; Purohit, A.; Chander, S.; et al. Thermal Annealing Evolution to Physical Properties of ZnS Thin Films as Buffer Layer for Solar Cell Applications. *Phys. E Low Dimens. Syst. Nanostructures* **2018**, *101*, 174–177.
20. Chen, S.; Song, L.; Zhang, P.; et al. Influence of Low-Temperature Sulfidation on the Structure of ZnS Thin Films. *Chin. Phys. B* **2019**, *28*, 024214.
21. Sharma, K.; Kumar, A.; Ahamad, T.; et al. Sulphur Vacancy Defects Engineered Metal Sulfides for Amended Photo (Electro) Catalytic Water Splitting: A Review. *J. Mater. Sci. Technol.* **2023**, *152*, 50–64.
22. Dai, P.; Li, W.; Xie, J.; et al. Forming Buried Junctions to Enhance the Photovoltage Generated by Cuprous Oxide in Aqueous Solutions. *Angew. Chem.* **2014**, *126*, 13711–13715.
23. Buckley, A.N.; Wouterlood, H.J.; Woods, R. The Surface Composition of Natural Sphalerites under Oxidative Leaching Conditions. *Hydrometallurgy* **1989**, *22*, 39–56.
24. Agostinelli, E.; Battistoni, C.; Fiorani, D.; et al. An XPS Study of the Electronic Structure of the Zn_xCd_{1-x}Cr₂(X = S, Se) Spinel System. *J. Phys. Chem. Solids* **1989**, *50*, 269–272.
25. Hu, S.; Jin, L.; Si, W.; et al. Sulfur Vacancies Enriched 2D ZnIn₂S₄ Nanosheets for Improving Photoelectrochemical Performance. *Catalysts* **2022**, *12*, 400.
26. Loget, G.; Mériadec, C.; Dorcet, V.; et al. Tailoring the photoelectrochemistry of catalytic metal-insulator-semiconductor (MIS) photoanodes by a dissolution method. *Nat. Commun.* **2019**, *10*, 3522.
27. Zhang, D.; Li, H.; Riaz, A.; et al. Unconventional Direct Synthesis of Ni₃N/Ni with N-Vacancies for Efficient and Stable Hydrogen Evolution. *Energy Environ. Sci.* **2022**, *15*, 185–195.
28. Zhang, D.; Pan, W.; Sharma, A.; et al. Over 14% Unassisted Water Splitting Driven by Immersed Perovskite/Si Tandem Photoanode with Ni-Based Catalysts. *Mater. Today Energy* **2025**, *48*, 101809.
29. Streetman, B.G.; Banerjee, S. *Solid State Electronic Devices New Jersey*; Prentice Hall: Upper Saddle River, NJ, USA, **2000**.
30. Wang, L.; Xia, L.; Wu, Y.; et al. Zr-Doped β-In₂S₃ Ultrathin Nanoflakes as Photoanodes: Enhanced Visible-Light-Driven Photoelectrochemical Water Splitting. *ACS Sustain. Chem. Eng.* **2016**, *4*, 2606–2614.
31. Cheiwchanchamnangij, T.; Lambrecht, W.R. Quasiparticle band structure calculation of monolayer, bilayer, and bulk MoS₂. *Phys. Rev. B Condens. Matter Mater. Phys.* **2012**, *85*, 205302.
32. Zhao, Z.; Cao, Y.; Yi, J.; et al. Band-Edge Electronic Structure of β-In₂S₃: The Role of s or p Orbitals of Atoms at Different Lattice Positions. *ChemPhysChem* **2012**, *13*, 1551–1556.